Hearing requires otoferlin-dependent efficient replenishment of synaptic vesicles in hair cells

Tina Pangrsic, Livia Lasarow, Kirsten Reuter, Hideki Takago, Martin Schwander, Dietmar Riedel, Thomas Frank, Lisa M Tarantino, Janice Bailey, Nicola Strenzke, et al.

Hearing requires otoferlin-dependent efficient replenishment of synaptic vesicles in hair cells

T. Pangršič[1], L. Lasarow[2], K. Reuter[3,*], H. Takago[1,*], M. Schwander[4], D. Riedel[5], T. Frank[1], L. M. Tarantino[6], J. S. Bailey[6], N. Strenzke[2], N. Brose[7], U. Müller[4], E. Reisinger[3], T. Moser[1,8]

[1]*InnerEarLab, Department of Otolaryngology and Center for Molecular Physiology of the Brain, University Medical Center Göttingen, Göttingen, Germany*

[2]*Auditory Systems Physiology, Department of Otolaryngology, University Medical Center Göttingen, Göttingen, Germany*

[3]*Molecular Biology of Cochlear Neurotransmission group, Department of Otolaryngology, University Medical Center Göttingen, Göttingen, Germany*

[4]*Department of Cell Biology, Institute for Childhood and Neglected Diseases, The Scripps Research Institute, La Jolla, California*

[5]*Laboratory of Electron Microscopy, Max Planck Institute for Biophysical Chemistry, Göttingen, Germany*

[6]*Department of Psychiatry, University of North Carolina, Chapel Hill, North Carolina*

[7]*Department of Molecular Neurobiology and Center for Molecular Physiology of the Brain, Max Planck Institute of Experimental Medicine, Göttingen, Germany*

[8]*Bernstein Center for Computational Neuroscience, University of Göttingen, Göttingen, Germany*

*equal contribution

Inner hair cell (IHC) ribbon synapses indefatigably transmit acoustic information. The proteins mediating their fast vesicle replenishment (hundreds of vesicles/s) are unknown. Here we show that an Asp to Gly substitution in the C_2F domain of the synaptic vesicle protein otoferlin impairs hearing by reducing vesicle replenishment in the *pachanga* mouse model of human deafness DFNB9. *In vitro* estimates of vesicle docking, the readily releasable vesicle pool (RRP), Ca^{2+} signaling and vesicle fusion were normal. Moreover, we observed postsynaptic excitatory currents of variable size and spike generation. However, mutant active zones (AZs) replenished vesicles at lower rates, and sound-evoked spiking in auditory neurons was sparse and only partially improved during longer inter-stimulus intervals. We conclude that replenishment does not keep up with release of vesicles at mutant AZs *in vivo*, such that a sufficient standing RRP cannot be maintained. We propose a novel role of otoferlin in replenishing synaptic vesicles.

At the first auditory synapse in mammals, one ribbon-type AZ of the IHC drives one postsynaptic spiral ganglion neuron (SGN) to spike at rates exceeding 100 Hz in silence and 1 kHz upon sound onset[1, 2]. Moreover, SGNs sustain firing rates of several hundred Hz during ongoing acoustic stimulation. In such a steady state, vesicle replenishment has to balance vesicle fusion at the IHC AZ. Accordingly, high rates of initial and sustained exocytosis have been found in hair cells[3–8]. Ribbon-type AZs of IHCs replenish readily releasable vesicles at hundreds of Hz over several seconds of stimulation, faster than ribbon synapses in the eye[9–15] and most non-ribbon-type AZs[16] (but see ref. 17). This efficient vesicle re-supply maintains a large standing pool of fusion competent synaptic vesicles, which appears to be critical for reliable and temporally precise sound encoding[18–20].

Ca^{2+} stimulates vesicle re-supply at presynaptic AZs[4, 8, 21, 22], yet the molecular basis underlying the unique replenishment capacity of IHCs remains unclear. One candidate for this function is the multi-C_2 domain protein otoferlin. Otoferlin has been implicated in synaptic vesicle fusion in IHCs[23], as Ca^{2+}-dependent exocytosis is largely abolished in IHCs of otoferlin knock-out mice (*Otof*$^{-/-}$), and has been shown to interact with SNARE proteins[23] and Myosin VI[24, 25].

Here, we studied the effects of a partial loss of otoferlin function from the molecular to the systems level using deaf *pachanga* mice (*Otof*$^{Pga/Pga}$)[26], which carry a N-ethyl-N-nitrosourea-mediated *Otof* missense mutation (D1767G in NP 001093865). We found reduced otoferlin protein levels in IHCs of *Otof*$^{Pga/Pga}$ mice. We explored synaptic transmission at the IHC synapse *in vitro* using pre- or postsynaptic patch-clamp, Ca^{2+} uncaging and Ca^{2+} imaging as well as *in vivo* by recording auditory evoked population responses and single neuron spiking. We present evidence that deficient vesicle replenishment underlies the hearing impairment of *Otof*$^{Pga/Pga}$ mice and propose that otoferlin confers the high capacity for vesicle re-supply to the IHC synapse.

Results

Normal cochlear function upstream of the IHC synapse

Otof$^{Pga/Pga}$ mice lacked auditory brainstem responses even when probed by very loud sounds (120 dB, **Fig. 1a**) but showed a small potential around the click stimulus, which probably reflected summed potentials of hair cells. We observed distortion products of otoacoustic emissions with normal amplitude (data not shown) corroborating the notion of intact cochlear amplification[26]. To further narrow down the site of defect we studied cochlear function by electrocochleography. Cochlear microphonics, reflecting hair cell mechanoelectrical transduction, were readily observed with amplitudes comparable to wild-type mice (*Otof*$^{+/+}$, **Fig. 1b**). The summating potential, thought to primarily reflect the summed IHC receptor potential, was maintained in *Otof*$^{Pga/Pga}$ mice (**Fig. 1c**, 48 ± 15 µV for *Otof*$^{+/+}$ and 44 ± 11 µV for *Otof*$^{Pga/Pga}$, n = 6 each), indicating that IHC transduction and basolateral conductance were normal. However, we did not observe obvious compound action potentials even at click stimulation of 130 dB (**Fig. 1d**). We conclude that the defect causing the hearing impairment of *Otof*$^{Pga/Pga}$ mice is located downstream of IHC receptor potential generation, most likely at the IHC synapse. We did not test auditory nerve function by electrical stimulation in *Otof*$^{Pga/Pga}$ mice but note that electrically evoked auditory brainstem responses were observed in *Otof*$^{-/-}$ mice[23].

Normal vesicle fusion but reduced replenishment

Next, we performed patch-clamp measurements of Ca^{2+} currents and membrane capacitance to study presynaptic function in apical IHCs of *Otof*$^{Pga/Pga}$, *Otof*$^{Pga/-}$, *Otof*$^{-/-}$ and *Otof*$^{+/+}$ mice (**Fig. 2a**–**b**). Unexpectedly, we found normal exocytic membrane capacitance increments (ΔC_m) for depolarizations lasting up to 10 ms in IHCs of *Otof*$^{Pga/Pga}$ and *Otof*$^{Pga/-}$ mice (**Fig. 2b**), indicating normal exocytosis of the RRP[4] at inter-stimulus intervals of at least 30 s. We then fitted the mean ΔC_m values obtained for different stimulus durations using the sum of an exponential and a linear function to

estimate the amount and kinetics of RRP exocytosis and the rate of sustained exocytosis, respectively (lines in **Fig. 2b**, fit results in **Table 1**)[4, 27]. This analysis revealed normal RRP size and exocytosis kinetics at AZs of *Otof*$^{Pga/Pga}$ mice (**Table 1**) in striking contrast to the near complete lack of RRP exocytosis in IHCs of *Otof*$^{-/-}$ mice (**Fig. 2a**–**b** and ref. 23), which showed significant exocytosis only for depolarization of 100 ms and longer ($p < 0.01$, data of ref. 23).

Moreover, Ca^{2+} uncaging caused a small fast ΔC_m in *Otof*$^{Pga/Pga}$ but not in *Otof*$^{-/-}$ IHCs (**Fig. 2c** and **Table 1**). Potential reasons for the drastic amplitude reduction of the flash photolysis-induced ΔC_m in *Otof*$^{Pga/Pga}$, which is still larger than the Ca^{2+} influx-triggered RRP exocytosis by one order of magnitude, could include fewer docked and primed vesicles outside AZs. The rate constants of the remaining fast component of *Otof*$^{Pga/Pga}$ IHCs at a given postflash $[Ca^{2+}]_i$ were comparable to those of *Otof*$^{+/+}$ IHCs, which is consistent with the notion of an unaltered Ca^{2+}-dependent fusion reaction (**Fig. 2c**, right panel and **Table 1**). Confocal Ca^{2+} imaging showed IHC synaptic Ca^{2+} microdomains[28] with normal amplitude and size as well as near normal kinetics (**Fig. 2d**–**f** and **Supplementary Table 1**). Therefore, we attribute the small reduction of the Ca^{2+} influx in *Otof*$^{Pga/Pga}$ IHCs (20 %, **Fig. 2a**–**b**) to the similarly decreased number of synapses (19%) assessed by immunohistochemistry (*Otof*$^{Pga/Pga}$: 10.4 ± 0.7 synapses per IHC, n = 357 IHCs vs. *Otof*$^{+/+}$: 12.8 ± 0.3 synapses per IHC, n = 180 IHCs; **Supplementary Fig. 1** and **Supplementary Table 2**). In summary, the above findings indicate that presynaptic Ca^{2+} signaling, RRP size and vesicle fusion are intact at AZs of *Otof*$^{Pga/Pga}$ IHCs under the chosen *in vitro* conditions.

However, beyond 10 ms of depolarization, the capacitance rise proceeded much more slowly in *Otof*$^{Pga/Pga}$ and *Otof*$^{Pga/-}$ IHCs. This sustained exocytosis after release of

the RRP is thought to primarily represent the rate-limiting re-supply of vesicles to the RRP and their subsequent fusion during continued Ca^{2+} influx[5, 8, 29–31], but a potential contribution of fusion-competent vesicles that are released more slowly cannot be completely ruled out. Here we assumed that sustained exocytosis primarily reports re-supply to the RRP and estimated its rate as the slope of the linear function fitted to the data of **Fig. 2b**. We conclude that mean vesicle supply is diminished from 700 vesicles/s per AZ in $Otof^{+/+}$ to 200 vesicles/s per AZ in $Otof^{Pga/Pga}$ and 100 vesicles/s per AZ in $Otof^{Pga/-}$ IHCs (**Fig. 2b** and **Table 1**). Increasing the Ca^{2+} influx even beyond that of $Otof^{+/+}$ IHCs by elevating the $[Ca^{2+}]_e$ enhanced sustained exocytosis in $Otof^{Pga/Pga}$ IHCs (360 vesicles/s per AZ). This indicated that the mutation does not abolish the Ca^{2+} dependence of vesicle supply and that the replenishment defect can be partially overcome by increasing Ca^{2+} influx.

The observations of normal RRP size after resting the synapse for more than 30 seconds and of reduced vesicle re-supply during ongoing stimulation prompted us to explore RRP recovery from depletion in paired-pulse experiments (**Fig. 3a**). RRP recovery, assessed as the paired-pulse ratio for different inter-pulse intervals, was impaired in $Otof^{Pga/Pga}$ mice (**Fig. 3b**). This indicated a deficit in vesicle replenishment also in the rest period between stimuli. The ΔC_m pattern elicited by trains of ten short (10 ms) depolarizations demonstrates the exocytosis phenotype found after a period of rest (30 s voltage-clamp at –84 mV): normal RRP exocytosis but subsequent failure (**Fig. 3c**). Studying the C_m decline after exocytosis we observed normal endocytic membrane retrieval (**Fig. 3d**).

Normal synaptic ultrastructure in $Otof^{Pga/Pga}$ IHCs

In order to explore whether a docking or a priming defect underlies the impairment of vesicle replenishment at $Otof^{Pga/Pga}$ IHC synapses, we studied their ultrastructure using electron microscopy (EM). Both, EM of single ultrathin sections (perpendicular to the

plasma membrane and the long axis of the ribbon; **Supplementary Fig. 2**) as well as EM tomography (**Fig. 3e–f**, **Supplementary Movies 1** and **2**) were performed. Organs of Corti were chemically fixed after either prolonged stimulation (40 mM $[K^+]_e$ and 5 mM $[Ca^{2+}]_e$) or inhibition (nominally Ca^{2+}-free, 5 mM $[EGTA]_e$ and 5 mM $[K^+]_e$) of exocytosis. We quantified the number of membrane-proximal vesicles ("docked", see below) and total ribbon-associated vesicles in electron micrographs of mid-synaptic ultrathin sections of each group (**Supplementary Fig. 2** and **Supplementary Table 3**). We found a significant reduction in the mean number of membrane-proximal vesicles per ribbon synapse section in stimulated synapses of both genotypes ($Otof^{+/+}$: 1.3 ± 0.2, $Otof^{Pga/Pga}$: 1.5 ± 0.1, n = 27 and 41 synapses, respectively) when compared to inhibiting conditions ($Otof^{+/+}$: 1.8 ± 0.1, $Otof^{Pga/Pga}$: 1.9 ± 0.1, n = 36 and 31 synapses, respectively; $p < 0.05$ for both genotypes). However, we did not detect significant differences between $Otof^{Pga/Pga}$ and $Otof^{+/+}$ IHC synapses in either inhibitory or stimulatory conditions (**Supplementary Fig. 2** and **Supplementary Table 3**).

High-resolution EM tomography (**Fig. 3e–f**) was used to measure the distance of membrane-proximal synaptic vesicles (labeled orange in **Fig. 3f**) from the plasma membrane under both conditions. The average membrane-membrane distance was approximately 6 nm regardless of condition and genotype (**Supplementary Table 3**), which is compatible with the notions that (1) the membrane-proximal vesicles were physically docked and (2) vesicle docking is intact at $Otof^{Pga/Pga}$ IHC synapses even during continuous strong stimulation. While we cannot completely rule out a trafficking/docking phenotype that may have been masked by strong stimulation compensating for the otoferlin defect, we favor that impaired priming underlies the defective vesicle replenishment.

Reduced rates but maintained size variability of EPSCs

The stark contrast between the absence of auditory neuron population responses *in vivo* (**Fig. 1**) and normal RRP exocytosis after sufficient resting reported by C_m measurements *in vitro* in *Otof*$^{Pga/Pga}$ mice led us to test postsynaptic function. We performed patch-clamp recordings from postsynaptic boutons of SGNs in *Otof*$^{Pga/Pga}$ mice at postnatal day 8–10. These measurements revealed the occurrence of excitatory postsynaptic currents (EPSCs) of variable size and shape, although at lower rates when compared to *Otof*$^{+/+}$ mice (**Fig. 4a**–**b**). We pooled the data from recordings in 5.8 and 40 mM $[K^+]_e$ as previous work[8, 32, 33] has demonstrated that the mean EPSC amplitude is stimulus-independent in rat SGNs. Like in immature rat SGNs we found a substantial fraction of multiphasic EPSCs in mice of both genotypes (10% of 644 EPSCs in *Otof*$^{+/+}$ and 16% of 279 EPSCs in *Otof*$^{Pga/Pga}$). Monophasic EPSCs of *Otof*$^{Pga/Pga}$ mice showed fast rise without obvious steps (see **Fig. 4d**–**e** for examples). The finding of large EPSCs with identical kinetics has been taken as evidence for highly synchronized multivesicular release[32]. The amplitude distribution of monophasic EPSCs was not significantly different in *Otof*$^{Pga/Pga}$ SGNs as compared to controls (**Fig. 4h**–**i**; Kolmogorov-Smirnov test, $p = 0.14$). Moreover, we detected action potential generation by recording action currents in the loose-patch configuration (**Fig. 4g**). Together these results suggest that *Otof*$^{Pga/Pga}$ synapses should be capable of encoding sound into spiking activity in auditory nerve fibers, albeit at lower rates.

In addition, we recorded from SGNs of *Otof*$^{-/-}$ mice of the same age and observed variably sized EPSCs at a very low rate (n = 5 *Otof*$^{-/-}$ SGNs, **Fig. 4c**), indicating that the observed ΔC_m in *Otof*$^{-/-}$ IHCs (ref. 23 and **Fig. 2**), indeed, reported synaptic transmitter release. We also observed action currents in the loose-patch configuration (**Fig. 4g**). In conclusion, transmitter release and postsynaptic spike

generation in SGNs occur in otoferlin mutants and EPSC variability is observed also in the absence of otoferlin.

Systems consequences of impaired vesicle replenishment

How can the partial defect at the ribbon synapse observed *in vitro* lead to such severe hearing impairment? We reasoned that spontaneous transmitter release in the absence of sound could steadily deplete the RRP in *Otof*$^{Pga/Pga}$ IHCs due to impaired vesicle supply. To test this hypothesis we performed extracellular recordings with microelectrodes targeted to the cochlear nucleus and the auditory nerve[34, 35]. Sound-driven single neuron activity was scarce and only found at high stimulus intensities (>100 dB SPL at 10 Hz). Broadband stimulation (white noise bursts) of sound-responsive neurons in *Otof*$^{Pga/Pga}$ mice revealed very low sound-driven spike rates, lacking the peak at sound onset typically observed in *Otof*$^{+/+}$ auditory nerve fibers and bushy cells (**Fig. 5a**). Sound-responsive neurons in *Otof*$^{Pga/Pga}$ mice – unlike in *Otof*$^{+/+}$ mice – could not be further classified into auditory nerve fibers and cochlear nucleus neurons based on their response properties[34]. Thus, we used data from putative auditory nerve fibers and bushy cells from *Otof*$^{+/+}$ mice as controls. Lowering stimulus rates (< 10 Hz) gradually improved sound onset responses (**Fig. 5b**, **Supplementary Fig. 3d**) and thresholds (**Supplementary Fig. 3b**) in *Otof*$^{Pga/Pga}$ neurons. We favor the interpretation that at lower stimulus rates vesicle supply can build up a standing RRP also at *Otof*$^{Pga/Pga}$ IHC synapses. In addition, there was a notable depression in the number of spikes occurring during the first trials of stimulation, especially at high stimulus rates in *Otof*$^{Pga/Pga}$ neurons (**Fig. 5c**), whereas such an adaptation was noted only at 10 Hz in *Otof*$^{+/+}$ neurons. Moreover, even at a rate of 1 Hz, 12% of the stimulus presentations failed to evoke spikes in *Otof*$^{Pga/Pga}$ neurons, while *Otof*$^{+/+}$ neurons always responded. Finally, *Otof*$^{Pga/Pga}$ neurons showed strongly increased latencies and jitter of the first spike for all inter-stimulus intervals (**Fig. 5d**). In summary, spiking at sound

onset occurred with low reliability and high temporal jitter in *Otof*$^{Pga/Pga}$ neurons probably not allowing summation into a sizable auditory population response[36] thereby explaining the absence of auditory evoked potentials (**Fig. 1**) even for increased inter-stimulus intervals (up to four seconds, data not shown). The distribution of spontaneous spike rates in *Otof*$^{Pga/Pga}$ neurons (mean rate: 4.7 ± 1.0 Hz) differed from *Otof*$^{+/+}$ auditory nerve fibers and cochlear nucleus units (23.9 ± 2.7 Hz) in that all units had spontaneous rates below 30 Hz (**Supplementary Figure 3a**). Irrespective of whether sound-responsive neurons in *Otof*$^{Pga/Pga}$ mice represented auditory nerve fibers or principal neurons of the cochlear nucleus, these *in vivo* data support the hypothesis of an auditory fatigue due to defective vesicle replenishment at the IHC synapses in *Otof*$^{Pga/Pga}$ mice.

Reduced otoferlin protein levels in *Otof*$^{Pga/Pga}$ IHCs

Next, we addressed potential molecular mechanisms by which the *pachanga* mutation could affect the function of otoferlin in vesicle priming. We first explored the levels of otoferlin mRNA and protein. Otoferlin mRNA levels assessed by real-time PCR were not significantly altered in *Otof*$^{Pga/Pga}$ (1.6 ± 0.2 -fold of *Otof*$^{+/+}$; n = 4, p = 0.11). Localization and protein levels of otoferlin were studied by quantitative optical microscopy of immunolabeled IHCs. We found overlapping distributions of Vglut3 (glutamate transporter of IHC synaptic vesicles[37–39]) and otoferlin immunofluorescence throughout the cytosol and along the plasma membrane, both in *Otof*$^{+/+}$ and *Otof*$^{Pga/Pga}$ IHCs. The latter, however, showed much weaker otoferlin immunofluorescence (**Fig. 6**). We quantified otoferlin protein levels using antibodies against N- and C-terminal epitopes, binding of both unlikely to be affected by the point mutation in the C_2F domain. In basolateral and apical IHC compartments otoferlin protein levels increased in the order of *Otof*$^{Pga/-}$ < *Otof*$^{Pga/Pga}$ < *Otof*$^{+/-}$ (**Fig. 6b**–**e**, **g**). *Otof*$^{-/-}$ mice (**Fig. 6f**–**g**) served as negative controls. Vglut3 immunofluorescence was decreased by

approximately 30% in all mutant phenotypes, indicating that the reduction in otoferlin immunofluorescence may in part be attributed to a reduction in synaptic vesicle number in these IHCs (**Fig. 6g**). Nonetheless, the reduced relative fluorescence (otoferlin/Vglut3) indicated that synaptic vesicles in *Otof*$^{Pga/–}$ and *Otof*$^{Pga/Pga}$ IHCs contain fewer copies of otoferlin. In addition, otoferlin immunofluorescence in *Otof*$^{Pga/Pga}$ IHCs was reduced more strongly at the plasma membrane than in the cytoplasm (**Supplementary Fig. 4a**).

We then tested the impact of the *pachanga* point mutation on the secondary structure of the otoferlin C_2F domain by circular dichroism (CD) spectroscopy. We observed slight changes in the CD-spectrum suggesting minor structural differences between wild-type and mutated C_2F domain (**Fig. 6h**). Adding Ca^{2+} to the protein solution had no effect on the CD-spectra of wild-type and mutated C_2F domains (**Fig. 6i**) nor on tryptophane autofluorescence of the wild-type C_2F domain (**Fig. 6j**). Moreover, we did not observe Ca^{2+}-dependent phospholipid binding (**Supplementary Fig. 4b**) for either the wild-type or the mutated C_2F domain. We conclude that lower protein levels of otoferlin potentially together with minor structural changes and impairment of protein-protein interactions, but not alteration of Ca^{2+} or phospholipid binding, contribute to the auditory phenotype of *Otof*$^{Pga/Pga}$ mice. Potential mechanisms for the lower otoferlin protein levels in *Otof*$^{Pga/Pga}$ IHC include a higher incidence of misfolding during protein synthesis leading to direct degradation and decreased protein stability resulting in faster degradation.

Discussion

The IHC ribbon synapse outperforms other synapses with respect to synaptic vesicle replenishment capacity. Here, we characterized the first known mutation that selectively affects this process in IHCs and identified otoferlin as a component of the underlying molecular machinery. The mutation impairs vesicle replenishment most likely by reducing otoferlin protein levels and potentially interfering with protein-protein interactions. Our analysis of *Otof*$^{Pga/Pga}$ IHC synapses indicates that compromised vesicle replenishment leads to auditory fatigue and profound hearing impairment, as a standing RRP of sufficient size cannot be maintained during synaptic activity *in vivo*.

We took advantage of the maintenance of Ca^{2+} influx-triggered fusion of readily releasable vesicles in the *Otof*$^{Pga/Pga}$ mutant[26]. Our results provide evidence for an additional function of otoferlin in vesicle priming (**Fig. 6k**) and argue against potential defects in vesicle trafficking and docking, synaptic Ca^{2+} signaling, fusion and transmitter release or endocytic membrane retrieval in *Otof*$^{Pga/Pga}$ IHCs. Currently we cannot exclude an impairment of AZ clearance after synaptic fusion[40] that would be functionally indistinguishable. A less likely interpretation of the reduced sustained exocytosis and smaller fast flash response would consider a major contribution of a slowly releasable pool of vesicles (docked at greater distance to Ca^{2+} channels[41] or using different Ca^{2+} sensor[42]) to sustained exocytosis and selectively impaired exocytosis of slowly releasable vesicles in *Otof*$^{Pga/Pga}$ IHCs.

Based on our *in vitro* recordings we conclude that a normal standing RRP can be established in *Otof*$^{Pga/Pga}$ IHCs, as long as enough time is provided for vesicle replenishment. Most likely, a normal number of 'slots' (close to Ca^{2+} channels[27, 43]) is available for releasable vesicles, which provide an intact Ca^{2+} influx-exocytosis coupling as indicated by normal RRP release kinetics. We favor the hypothesis that, *in vivo,* ongoing exocytosis in the absence of sound stimulation leads to steady vesicle

consumption and thus a smaller standing RRP in *Otof*$^{Pga/Pga}$ IHCs. This reduced RRP and the slower speed of vesicle supply probably limit the rates of transmitter release and subsequent neuronal spiking upon sound stimulation.

In addition to accelerating vesicle replenishment, otoferlin has been implicated in Ca^{2+}-triggered fusion[23]. Does otoferlin then assume multiple functions in IHC exocytosis? In the absence of otoferlin a stronger impairment in vesicle replenishment than observed in *Otof*$^{Pga/Pga}$ IHCs could arise. However, the complete lack of fast exocytosis even after long periods of rest together with partially preserved slow exocytosis in *Otof*$^{-/-}$ IHCs cannot simply be explained this way and rather indicates an additional requirement for otoferlin in fusion[23] (**Fig. 6k**). Whereas in *Otof*$^{-/-}$ IHCs the perturbation of vesicle replenishment and fusion causes a complete loss of fast exocytosis, the functionality of the *pachanga* mutant protein and the number of protein copies present on synaptic vesicles apparently suffice to support fast fusion in IHCs, but fail to maintain efficient vesicle replenishment. Regarding this dual-function hypothesis for otoferlin it is noteworthy that a function upstream of fusion was recently also reported for synaptotagmin 1[44].

Otoferlin, which seems to be absent from other synapses such as retinal ribbon synapses[35], is an attractive candidate for conferring the fast vesicle replenishment capacity to IHCs. During strong *in vitro* stimulation, IHCs sustain a near constant exocytosis rate of hundreds (700 in the present study) of vesicles/s per AZ or tens of vesicles/s per 'RRP slot' for at least one second during ongoing stimulation. The vesicle supply rates of wild-type IHCs exceed those of rat retinal bipolar cells by almost an order of magnitude (70 vesicles/s per AZ), despite comparable synaptic ultrastructure and RRP size of bipolar cell AZs[14]. Estimates of maximal vesicle supply in retinal photoreceptors of the salamander, which feature larger AZs than IHCs and bipolar cells[45], amount to approximately 200 vesicles/s per AZ[13, 15]. Interestingly, sustained

exocytosis of mouse vestibular hair cells operates at lower rates than in cochlear IHCs and is reduced upon deletion of otoferlin[46]. Different rates of vesicle supply and different effects of otoferlin deletion in auditory and vestibular hair cells might reflect the involvement of distinct proteins that co-determine the replenishment rate. Different from retinal and vestibular junctions, each postsynaptic auditory neuron is driven by a single IHC AZ and fires up to hundreds of Hz during ongoing acoustic stimulation (for review, see ref. 2) requiring similar or higher rates of release.

How can one reconcile substantial sustained exocytosis (200 vesicles/s per active zone) observed in IHCs of *Otof*$^{Pga/Pga}$ mice *in vitro* with the severe impairment of sound encoding *in vivo*? If other aspects of cochlear function apart from vesicle replenishment are intact as indicated by normal otoacoustic emissions, cochlear microphonics, and summating potentials, then why were high sound pressure levels required to elicit neuronal responses? While alternative interpretations cannot be ruled out at present, we favor the hypothesis that the requirement for otoferlin may be most critical for maintaining a standing RRP during weak stimulation. The Ca^{2+} signal elicited by strong stimulation: saturating depolarizations and elevated $[Ca^{2+}]_e$ (**Fig. 2**), high $[K^+]_e$ (**Figs. 3** and **4**) and high sound intensities (**Fig. 5**) might have been high enough to enhance vesicle supply and support substantial transmission even in *Otof*$^{Pga/Pga}$ mice. It is tempting to speculate that the multi-C_2-domain protein otoferlin endows vesicle supply at the IHC synapse with high Ca^{2+} sensitivity to enable sufficient vesicle replenishment also during weak stimulation. Future studies are required to further characterize the Ca^{2+} dependence of vesicle supply in IHCs.

Supplementary Information is available on the Nature Neuroscience website.

Acknowledgments We would like to thank E. Glowatzki and D. Khimich for teaching us the postsynaptic patch-clamp, K. Tittman, D. Fasshauer and R. Jahn for advice and support for protein biochemistry, C.P. Richter and M.A. Cheatham for advice on the electrocochleography, A. Leonov and C. Griesinger for the DM-nitrophen, P. Jonas for the parvalbumin taqman probe, members of the InnerEarLab for discussion, M. Rutherford, J. Singer, E. Neher, J. Siegel, P. Heil, T. Sakaba, R. Nouvian, A. Lysakowski and A. Lee for comments on the MS, and C. Rüdiger, S. Blume, N. Dankenbrink-Werder and M. Köppler for expert technical assistance. This work was supported by a fellowship of the Alexander von Humboldt Foundation to T.P., a fellowship of the Boehringer Ingelheim Fonds to K.R., a fellowship of MED-EL company to H.T., grants of the DFG (Center for Molecular Physiology of the Brain, T.M. and N.B.; Fellowship to N. Strenzke), the EC (Eurohear, T.M.), of the Max-Planck-Society (Tandemproject, T.M. and N.B.), BMBF (Bernstein Center for Computational Neuroscience Goettingen, T.M.), the State of Lower Saxony ("VW-Vorab" to T.M. and Christoph Matthias), and the National Institute of Health (DC007704, U.M.).

Author Contributions The study was designed by T.M., T.P., U.M., N.S., E.R. & N.B. The experimental work was performed by T.P. (IHC patch-clamp and flash photolysis, extracellular postsynaptic recordings, immunohistochemistry, contribution to EM), L.L. (*in vivo* single unit recordings, electrochcochleography and ABR), K.R. (Real-Time PCR, protein purification, CD spectroscopy, fluorimetry and floatation assay), H.T. (postsynaptic recordings), M.S. (ENU screen and initial auditory testing), D.R. (electron microscopy), T.F. (Ca^{2+} imaging), N.S (*in vivo* physiology), E.R. (generation of KO), J.S.B. & L.M.T. (started ENU screen). T.M. and T.P. prepared the MS.

Author Information Correspondence and requests for materials should be addressed to T.M. (tmoser@gwdg.de) or E.R. (ereisin@gwdg.de).

Figure Legends

Figure 1 Normal hair cell transduction and receptor potentials in *Otof*$^{Pga/Pga}$ mice but severe hearing impairment

a, no auditory brainstem responses (ABR) were elicited by 120 dB (top) and 80 dB (bottom) click stimuli in *Otof*$^{Pga/Pga}$ mice aged 2–4 weeks (average trace), whereas normal responses were seen in *Otof*$^{+/+}$ (representative examples) animals. **b,** electrocochleography: representative traces in response to 12 ms 90 dB 12 kHz tone bursts (indicated by top trace) recorded at high bandwidth illustrating the presence of large cochlear microphonics in an *Otof*$^{Pga/Pga}$ and an *Otof*$^{+/+}$ mouse. The spiral ganglion compound action potential (CAP, visible for *Otof*$^{+/+}$ at the onset of the tone) is missing in the *Otof*$^{Pga/Pga}$ mouse. **c,** averages (± SEM) of low-pass filtered (3 kHz) electrocochleography traces in response to 12 ms 90 dB 12 kHz tone bursts for *Otof*$^{Pga/Pga}$ and *Otof*$^{+/+}$ mice: normal summating potential (SP), but lack of CAP in *Otof*$^{Pga/Pga}$ mice. **d,** for clicks at a stimulus level of 130 dB, a small putative negative potential becomes apparent (arrow) in the *Otof*$^{Pga/Pga}$ mice (n = 3), potentially representing a residual spiral ganglion CAP (absent for 90 dB click stimulation).

Figure 2 Normal vesicle fusion but impaired vesicle replenishment in *Otof*$^{Pga/Pga}$ IHCs

a, representative Ca^{2+} currents (top) and low-pass filtered C_m changes (bottom) recorded from *Otof*$^{+/+}$, *Otof*$^{Pga/Pga}$ and *Otof*$^{-/-}$ IHCs in response to 20 ms (left) and to 100 ms (right) depolarizations. **b**, mean (± SEM) exocytic ΔC_m (top) and Ca^{2+} current integrals

(bottom) of *Otof*$^{+/+}$ (n = 8), *Otof*$^{Pga/Pga}$ (n = 14), *Otof*$^{Pga/-}$ (n = 13) and *Otof*$^{-/-}$ (n = 7) IHCs as a function of stimulus duration. In addition, data of *Otof*$^{Pga/Pga}$ IHCs bathed in elevated $[Ca^{2+}]_e$ (10 mM, n = 7) are shown. Lines represent least-square fits to the data (see **Table 1**). Inset shows the first 20 ms on an expanded scale. **c,** average ΔC_m traces (± SEM) of *Otof*$^{+/+}$ (n = 7), *Otof*$^{Pga/Pga}$ (n = 10) and *Otof*$^{-/-}$ (n = 7) IHCs recorded during Ca^{2+} uncaging (0 ms indicates time of flash; see **Table 1** for fit parameters). Right panel: rate constants of the fast exocytic component as a function of postflash $[Ca^{2+}]_i$ in *Otof*$^{Pga/Pga}$ and wild-type IHCs (*Otof*$^{+/+}$; a – present data, b – taken from ref. [47]). The line represents the fit of a fifth-order model with a cooperativity factor of 0.4 (see ref. [47]). **d,** representative hotspots of Fluo-5N fluorescence (Ca^{2+} microdomains) in IHCs of *Otof*$^{+/+}$ and *Otof*$^{Pga/Pga}$ mice during depolarization to –7mV. Scale bar: 2 µm. **e,** means and SD of background-subtracted Fluo-5N fluorescence recorded by spot-detection in the center of the Ca^{2+} microdomain[28] (81 domains in 23 *Otof*$^{+/+}$ IHCs [black line and dark grey area] and 88 domains in 24 *Otof*$^{Pga/Pga}$ IHCs [grey dashed line and light grey area]). **f,** distribution of Ca^{2+} microdomain peak ΔF of the same IHCs.

Figure 3 Fatigue of exocytosis, slowed RRP refilling, but unaltered docking and endocytic membrane retrieval

a, representative ΔC_m traces (top) and Ca^{2+} currents (bottom) obtained in *Otof*$^{+/+}$ and *Otof*$^{Pga/Pga}$ IHCs in response to a pair of 20 ms long depolarizations to –14 mV, which were separated by 89 ms. **b,** mean ratios of exocytic ΔC_m (± SEM) in response to the second depolarization (ΔC_{m2}) over the first (ΔC_{m1}) as a function of inter-stimulus interval for *Otof*$^{+/+}$ (n = 13) and *Otof*$^{Pga/Pga}$ (n = 15) IHCs. **c,** average ΔC_m traces

recorded in response to 8 Hz trains of 10 ms depolarizations in *Otof*$^{+/+}$ and *Otof*$^{Pga/Pga}$ IHCs. **d,** endocytic membrane capacitance changes measured in response to 20 ms depolarization pulses to peak Ca^{2+} current potential at 2 mM $[Ca^{2+}]_e$ in *Otof*$^{Pga/Pga}$ (n = 5) and in *Otof*$^{+/+}$ IHCs (n = 12). In an additional data set, 11 *Otof*$^{Pga/Pga}$ IHCs acquired in 10 mM $[Ca^{2+}]_e$, also showed robust endocytosis (data not shown). **e,** tomogram sections of ribbon synapses in *Otof*$^{+/+}$ (left) and *Otof*$^{Pga/Pga}$ (right) IHCs fixed in stimulatory conditions. **f,** 3-D model of an *Otof*$^{Pga/Pga}$ synapse fixed in stimulatory conditions seen from the synaptic cleft (left) and the side (right). Scale bar: 100 nm.

Figure 4 Synchronized multivesicular release and spike generation in otoferlin mutants

a–c, whole-cell voltage-clamp recordings of postsynaptic EPSCs in representative *Otof*$^{+/+}$ (**a**), *Otof*$^{Pga/Pga}$ (**b**) and *Otof*$^{-/-}$ (**c**) boutons. Bar indicates the bath perfusion of stimulatory 40 mM K^+ saline evoking EPSCs at a reduced rate but with size variability in *Otof*$^{Pga/Pga}$ (note different time scale in **c**). **d–f,** enlarged absolute (top) and normalized (bottom) EPSCs: kinetically homogeneous but variably sized EPSCs. **g,** action currents recorded from terminals of *Otof*$^{Pga/Pga}$ (top) and *Otof*$^{-/-}$ (bottom) mice. **h,** pooled amplitude distributions for monophasic EPSCs of all *Otof*$^{+/+}$ and *Otof*$^{Pga/Pga}$ boutons (n = 6 cells 577 EPSCs and n = 4 cells 235 EPSCs, respectively). Bin width in the histogram is 5 pA. **i,** Cumulative amplitude distributions do not show significant difference in average EPSC size for the two genotypes.

Figure 5 Reduced and fatiguing sound encoding in *Otof*$^{Pga/Pga}$ mice

a, mean poststimulus time histograms (± SEM) of auditory nerve fibers (AN, n = 15, primary-like discharge pattern, depth >1000 μm from the surface of the cochlear nucleus) and bushy cells (BC, n = 34, primary-like type response with a depth of <1000 μm or primary-like with notch discharge pattern) obtained from responses to 10 Hz tone bursts at characteristic frequency 30 dB above threshold in *Otof*$^{+/+}$ mice and sound-responsive neurons recorded from the region of the cochlear nucleus: in *Otof*$^{Pga/Pga}$ mice (n = 10; 10 Hz noise bursts at 120–140 dB SPL). **b,** poststimulus time histograms of *Otof*$^{Pga/Pga}$ units stimulated at different rates (0.5–4 Hz, n = 8–13). **c,** the number of sound-evoked spikes during the first 50 trials of stimulation in *Otof*$^{Pga/Pga}$ (n = 15) and *Otof*$^{+/+}$ (n = 15) units. **d,** mean and SD of first spike latency in *Otof*$^{Pga/Pga}$ (n = 14) and *Otof*$^{+/+}$ (n = 12) units.

Figure 6 The *pachanga* mutation causes a reduction in otoferlin protein levels and a change in secondary structure

a–f, projected confocal sections of apical cochlear turns of different genotypes following immunolabeling for otoferlin (N-terminal, a–f, green) and Vglut3 (shown only in a, red) processed under identical conditions. Scale bar: 5 μm. **g,** fluorescence intensity averaged over an apical and a basal cytosolic region in either channel for the different genotypes. **h–i,** CD spectroscopy of purified wt and *pachanga* C_2F domains, (**h**) averaged traces (± SEM) in the presence of EDTA and (**i**) sample traces in the presence of EDTA or Ca^{2+}. **j,** tryptophane autofluorescence of purified wt C_2F domain, single traces in the presence of EDTA, Ca^{2+} and Mg^{2+}. **k,** proposed functions of

otoferlin in hair cell exocytosis: Priming is the proposed site of defect in *Otof*$^{Pga/Pga}$ mice, while docking, stabilization of a normal RRP (under release-inhibiting conditions), Ca^{2+}-triggered fusion, EPSC and spike generation, and endocytic membrane retrieval seem to function normally in *Otof*$^{Pga/Pga}$ IHCs. If, however, consumption due to spontaneous and evoked release is as high as *in vivo*, a standing RRP cannot be maintained in *Otof*$^{Pga/Pga}$ IHCs (grey ellipse vs. black ellipse). Based on this and previous work[23], otoferlin and Ca^{2+} are suggested to act on both vesicle priming and fusion.

Table 1 Quantification of exocytosis

Parameters of depolarization-induced exocytosis were estimated by least-square fitting of the following function:

$$\Delta C_m(t) = RRP\_size \cdot \left(1 - e^{-t/\tau}\right)^n + slope \cdot t,$$

where t denotes the duration of depolarization and τ the time constant for RRP depletion. The RRP size (in vesicles per active zone [AZ]) was estimated as the amplitude of the exponential function (in fF) divided by the product of synapse number and vesicle capacitance (~ 45 aF[48]). Initial and sustained rates of exocytosis (in vesicles/s per AZ) were calculated from the capacitance data as follows:
Initial rate = RRP_size (in fF) / No. of synapses / vesicle capacitance / τ,
Sustained rate = slope / No. of synapses /vesicle capacitance.
Vesicles in electron micrographs from *Otof*$^{+/+}$ and *Otof*$^{Pga/Pga}$ mice were of comparable size (data not shown).
Parameters of exocytosis during Ca^{2+} uncaging were estimated by least-square fitting of the following functions:

$$\Delta C_m(t) = a_1 \cdot \left(1 - e^{-(t-delay)/\tau_1}\right) + a_2 \cdot \left(1 - e^{-(t-delay)/\tau_2}\right)^n$$

for *Otof*$^{+/+}$ and *Otof*$^{Pga/Pga}$ data and

$$\Delta C_m(t) = a_2 \cdot \left(1 - e^{-t/\tau_2}\right)^n$$

for *Otof*$^{-/-}$ data. Data are presented as mean ± SEM (where available).

Depolarization						
	RRP_size (fF, entire IHC) (vesicles per AZ)	**τ-depletion** (ms)	**Initial rate** (vesicles/s per AZ)	**Slope** (fF/s, entire IHC)	**Sustained rate** (vesicles/s per AZ)	**Exponent n**
Otof $^{+/+}$ (n=8)	7.0 12	5.2	2344	391	679	2.9
Otof $^{Pga/Pga}$ (n=14)	6.4 14	3. 9	3495	98	208	1.6
Otof $^{Pga/Pga}$ (n=7) 10 mM Ca^{2+}	9.4 20	2.8	7117	167	357	2.1
Otof $^{Pga/–}$ (n=13)	6.1 13	4.5	2901	45	97	1.2
Ca^{2+} uncaging						
	delay (ms)	**a_1** (fF)	**τ_1** (ms)	**a_2** (fF)	**τ_2** (ms)	**[Ca^{2+}]** (μM) **n**
Otof $^{+/+}$ (n=7)	1.5 ± 0.5	1117 ± 144	5.4 ± 1.1	631 ± 127	26 ± 5	28 ± 3 1.7 ± 0.5
Otof $^{Pga/Pga}$ (n=14)	0.7 ± 0.1	78 ± 11	2.0 ± 0.3	182 ± 8	44 ± 4	43 ± 4 2.9 ± 0.2
Otof $^{–/–}$ (n=7)	–	–	–	150 ± 13	52 ± 9	52 ± 5 3.1 ± 0.5

Methods

Animals

Mice aged 1 (postsynaptic patch-clamp), 2–3 (presynaptic patch-clamp and immunohistochemistry) and 3–5 weeks (*in vivo* auditory physiology) were used. The generation of *Otof*$^{-/-}$ mice will be described elsewhere (Reisinger et al.; in preparation), that of *Otof*$^{Pga/Pga}$ is described in ref. 26. C57BL/6 mice were used as control animals. Animal handling and experiments complied with national animal care guidelines, and were approved by the University of Goettingen Board for animal welfare and the animal welfare office of the state of Lower Saxony.

Patch-clamp recordings

IHCs from the apical coils of freshly dissected organs of Corti were patch-clamped in the perforated-patch (depolarizations) or whole-cell (flash photolysis, Ca^{2+} imaging) configuration as described[4, 47]. The pipette solutions for perforated-patch experiments contained (in mM): 130 Cs-gluconate, 10 Tetraethylammonium-chloride (TEA-Cl), 10 4-aminopyridine (4-AP, Merck, Darmstadt, Germany), 1 $MgCl_2$, 10 Cs-HEPES (pH 7.17), 300 µg/ml amphotericin B (Calbiochem, La Jolla, CA). The pipette solution for flash-photolysis contained (in mM): 120 Cs-gluconate, 20 TEA-Cl, 20 Cs-HEPES (pH 7.2), 0.3 mag-fura-2 (Invitrogen, Karlsruhe, Germany), 10 DM-nitrophen (gift of A. Leonov and C. Griesinger, Göttingen), 5 DPTA (1,3-diaminopropan-2-ol-tetraacetic acid) and 10 $CaCl_2$. The pipette solution for Ca^{2+} imaging contained (in mM): 126 Cs-glutamate, 13 TEA-Cl, 20 Cs-HEPES, 1 $MgCl_2$, 0.1 $CaCl_2$, 2 MgATP, 0.3 NaGTP, 2 EGTA, 0.4 Fluo-5N (Penta-K^+ salt, Invitrogen), pH 7.0. The extracellular solutions contained (in mM): 113 NaCl (102 for Ca^{2+} imaging), 35 TEA-Cl, 2.8 KCl, 2 $CaCl_2$ (10

for flash-photolysis and most perforated-patch experiments, 5 for Ca^{2+} imaging), 1 $MgCl_2$, 10 Na-HEPES, 1 CsCl, 11.1 D-glucose (pH 7.2).

Loose-patch and whole-cell recordings from postsynaptic boutons were performed as described[32] using pipettes with small tip-opening (8–15 MΩ following pressure polishing[49]), a pipette solution containing (in mM): 150 KCl, 3.5 $MgCl_2$, 0.1 $CaCl_2$, 5 EGTA, 5 K-HEPES, 2.5 Na_2ATP, pH 7.2, and an extracellular solution containing (in mM): 5.8 KCl, 155 NaCl, 0.9 $MgCl_2$, 1.3 $CaCl_2$, 0.7 NaH_2PO_4, 5.6 D-glucose, 10 Na-HEPES, pH 7.4. In most recordings tetrodotoxin (1–2 μM) was added to block voltage-gated sodium channels. All chemicals were obtained from Sigma-Aldrich (Taufkirchen, Germany) unless stated otherwise. EPC-9 or EPC-10 amplifiers (HEKA Electronics, Lambrecht, Germany), controlled by Pulse or Patchmaster software, were used to sample and filter currents at 20 kHz and 5 kHz, respectively. We measured ΔC_m as previously described[4] using depolarizations of different durations to peak Ca^{2+} current potential at intervals of 30 to 60 s. ΔC_m were estimated as the difference of the mean C_m after depolarization and the mean pre-pulse C_m (the initial 40 ms after the depolarization were skipped). Mean ΔC_m and Ca^{2+} current estimates present grand averages calculated from the mean estimates of individual IHCs. In paired-pulse experiments we used two 20 ms-long pulses with variable inter-stimulus interval: 89, 154, 504 ms and 30 s. Currents were leak-corrected using a P/6-protocol. Recordings were performed at room temperature. Flash photolysis was performed as described[47].

Confocal imaging of Ca^{2+} signals at hair cell ribbon synapses

Confocal Ca^{2+} imaging was performed as previously described[28]. Ca^{2+} microdomains were identified in xy-scans during 200 ms long depolarizations and further

characterized using spot detection ("point scan" mode of the confocal scanner). During spot detection measurements the output of the photomultiplier tube (PMT) signal (500 kHz) was temporally averaged to yield an effective sampling rate of 1.85 kHz. Isochronal spot detection measurements were made at the center of a Ca^{2+} microdomain as well as at the 4 directly neighboring pixels on each side of the center along each direction of the X- and Y-axis (130 nm spacing between the neighboring recording locations and the center), each averaged 5 times. Only the maximum amplitude response was further analyzed. PMT dark current (measured with shutter closed) was subtracted for all measurements. Igor Pro (Wavemetrics, Lake Oswego, OR) was used for analysis.

Recordings of cochlear potentials (electrocochleography), ABRs and single unit responses

ABR recordings were performed as described[43].

For **electrocochleography**, the mouse head was fixed, the bulla was opened from a retroauricular incision, a silver ball-electrode was placed into the round window niche and the difference potential to a subdermal needle at the vertex was amplified (50 times, custom-built amplifier) and sampled at a rate of 50 kHz for 20 ms. For analysis of CAP (compound action potentials) and SP (summating potentials), responses to stimuli of inverting polarity were averaged and low-pass filtered (3 kHz) offline using Matlab (Mathworks, Natick, MA) software.

Single auditory neuron responses from the ventral cochlear nucleus (VCN) and auditory nerve were performed essentially as described in ref. 35. Upon audio-visual detection of spiking activity, units were further characterized by determining their spontaneous rate and responses to 50 ms noise bursts presented at 0.5, 1, 2, 4 or 10 Hz.

Attempts to record tuning curves did not yield consistent results in *Otof*$^{Pga/Pga}$ mice because of low spike rates that depended on interstimulus intervals, high thresholds (usually above 100 dB SPL) and broad frequency tuning. Subsequent offline spike detection using Matlab was based on amplitudes, waveform reproducibility and signal to noise ratio.

We assume we recorded mainly from primary units of the cochlear nucleus because:

- they were localized in the auditory nerve/cochlear nucleus region (many of them were too superficial to be auditory nerve fibers)
- signal to noise ratio and our ability to achieve long recording durations were relatively good, better than in typical auditory nerve recordings
- responses to low-frequency sounds (0.1–2 kHz) were not better than to higher-frequency sounds, arguing against a vestibular origin
- responses of individual units did not change after removal of whiskers, arguing against a trigeminal origin.

Spontaneous or sound-evoked responses also differed from wildtype olivocochlear efferents or vestibular neurons[50]. If we indeed recorded from such units, their responses must also have been affected by the mutation.

Immunostaining and confocal microscopy

Immunostaining was performed as previously described[18]. The following antibodies were used: mouse IgG1 anti-Ctbp2 (BD Biosciences, Heidelberg, Germany, 1:200), rabbit anti-GluR2/3 (Chemicon, Schwalbach, Germany, 1:200), mouse anti-calbindin (Swant, Bellinzona, Switzerland, 1:500), mouse anti-otoferlin (N-terminal, Abcam, Cambridge, UK, 1:500), rabbit anti-otoferlin (C-terminal, Synaptic Systems, Göttingen,

Germany, 1:500), rabbit anti-Vglut3 (Synaptic Systems, 1:500) and secondary AlexaFluor488- and AlexaFluor568-labeled antibodies (Invitrogen, 1:200). For 3D reconstructions of the specimen, z-axis stacks of 2D images were taken with a step size of 0.5 µm. They are shown in z-projections, done in ImageJ. Otoferlin and Vglut3 immunofluorescence signals were analyzed in apical and basolateral intracellular regions in maximum projections of confocal IHC sections. They were acquired at identical microscope settings and following parallel immunolabelling with the same procedure used for all genotypes.

Electron microscopy

The organs of Corti (apical cochlear coils) were explanted and exposed to stimulatory or inhibitory conditions for 10–15 min. For stimulation they were incubated in a depolarizing saline (containing in mM: 50 KCl, 95 NaCl, 1 $MgCl_2$, 5 $CaCl_2$, 10 HEPES, 11.1 D-glucose; pH 7.2, osmolarity approx. 300 mOsm) at room temperature. For inhibition the tissue was incubated in a Ca^{2+} free saline (containing in mM: 5 KCl, 140 NaCl, 3 $MgCl_2$, 5 EGTA, 10 HEPES, 11.1 D-glucose; pH 7.2, osmolarity approx. 300 mOsm) on ice. Thereafter, organs of Corti were incubated for 15–20 min in the respective solution now supplemented with 4 % glutaraldehyde (Electron Microscopy Sciences, Hatfield, PA) at room temperature. Afterwards, they were incubated overnight at 4°C in 0.1 M cacodylate buffer supplemented with 4 % glutaraldehyde. After an additional fixation in 0.1% OsO_4 the samples were stained with 1% uranyl acetate, dehydrated in a series of EtOH and finally in propylene oxide. They were then embedded in Agar 100 (purchased through Science Services, Munich, Germany). Thin sections (80 nm) were counterstained with lead citrate and examined using a Philips CM

120 BioTwin transmission electron microscope (Philips Inc., Eindhoven, Netherlands). Pictures were taken with a TemCam F224A camera (TVIPS, Gauting, Germany) at 20,000-fold magnification.

Quantitative image analysis was performed in iTEM software (Olympus), where we counted:

1. ribbon-associated synaptic vesicles: first row of vesicles around the ribbon with less than a vesicle diameter distance from the ribbon surface,
2. membrane-proximal vesicles: synaptic vesicles associated with the AZ within a membrane distance of max. 12 nm from the plasma membrane,
3. clathrin-coated vesicles.

To compare the number of membrane-proximal vesicles among the genotypes and among stimulatory and inhibitory conditions we performed permutation tests and Mann-Whitney U tests.

Electron Tomography

Sections (200 nm thick) of Agar 100 embedded organs of Corti were decorated with 10 nm colloidal gold particles on both surfaces. Tilt series (unidirectional tilt) were then recorded on a Philips CM120 transmission electron microscope (Philips Inc.Eindhoven, The Netherlands) at 27,500× magnification using a TVIPS 224A slow scan CCD camera in unbinning mode. The series were calculated using Etomo and the model was then created using Imod program (http://bio3d.colorado.edu/).

The smallest distance of membrane-proximal vesicles (outer leaflet) to the plasma membrane (inner leaflet) was quantified in the section displaying the closest proximity.

Protein biochemistry

The C_2F domain (amino acids 1688 to 1927 (NPDK…NEPD)) was subcloned as a GST-fusion construct into a pGEX-2T vector. For the pachanga variant, the point mutation was introduced by overlap-PCR using the oligonucleotides 5'-GCCAGCAGGAGGGCAAACAGGACACAGAC-3' and 5'-GTCTGTGTCCTGTTTGCCCTCCTGCTGGC-3'. The subcloned C_2F domains were verified by DNA sequencing. Protein expression in BL21-DE3 cells at 16°C (overnight) and purification of both constructs were performed in parallel. Cells were pelleted at 5,250 rcf and re-suspended in 20 mM Tris HCl pH 7.4, 500 mM NaCl, 2.5 mM reduced glutathione, 5 μM ATP and 5% EtOH. Then cells were lysed by sonication with a Branson sonifier 250. Cell debris was pelleted at 23,000 rcf and the protein was purified from the supernatant using Glutathione Sepharose^{TM} 4B. The protein was cleaved from the GST-tag with 10 U/ml thrombin overnight, while the tag remained bound to the sepharose beads. The protein solution was dialysed against 20 mM PB pH 7.4 (for EDTA runs in **Fig. 6h**) or 5 mM Tris pH 7.4 (for EDTA and Ca^{2+} runs in **Fig. 6i**–**j**) at 4°C, which had been pre-treated with Chelex100 (BioRad, Munich, Germany). Protein concentration was determined by UV-absorbance at 280 nm.

CD spectroscopy was performed on a Chirascan instrument (Applied Photophysics, Surrey, UK) at 25°C with a protein concentration of 0.08 mg/ml (3 μM) per run. EDTA or Ca^{2+} was added to a final concentration of 100 μM, respectively. Ellipticity was measured from 190 nm to 260 nm, controlling for sufficient light transmission by measuring high tension voltage. All spectra were corrected for buffer contributions.

Autofluorescence was measured in a Fluoromax-3 instrument (Jobin Yvon Horiba) with a protein concentration of 2.36 μM with 295 nm excitation wave length. Fluorescence emission was recorded from 305 – 450 nm in 1 nm steps with an integration time of 0.2 s, averaging 5 runs. Ca^{2+} or EDTA was added to a final concentration of 100 μM, respectively.

Real-Time PCR

The apical turns of 3–4 organs of Corti of *Otof*$^{Pga/Pga}$ or *Otof*$^{+/+}$ animals at P14 were dissected and mRNA was extracted by Trizol method. This was repeated three more times for each genotype independently. cDNA synthesis was performed using Superscript II reverse transcriptase in supplied buffer with Oligo dT and random hexamers as primers. Real-Time PCR was conducted in triplicates for each cDNA sample using an Applied Biosystems SDS 7500 thermal cycler and TaqMan Gene Expression Assays for otoferlin (Applied Biosystems, Darmstadt, Germany, Mm00453306_m1), and for the housekeeping genes parvalbumin (kindly provided by P. Jonas, Freiburg) and TATA binding protein (Mm00446973_m1). To average C_t values from triplicate experiments, we first calculated a linear value from each C_t value ($lin = 2^{-Ct}$). These linear values were averaged and back-transformed into a C_t value ($C_{t,\,average} = -LN\,(lin_{average}) / LN2$). Data were analyzed by $\Delta\Delta C_t$ method.

Data analysis

Data analysis was performed using Matlab, Igor Pro and ImageJ software. Figures were assembled for display in Adobe Photoshop and Illustrator software. Unless otherwise noted, data are expressed as mean ± SEM. Student's unpaired, two-tailed t-test was used to compare two samples (* indicates $p < 0.05$) unless stated otherwise.

References

1. Kiang, N.Y.-S., Watanabe, T., Thomas, E.C. & Clark, L.F. *Discharge pattern of single fibers in the cat's auditory nerve.* (MIT Press, Cambridge, Mass., 1965).
2. Geisler, C.D. *From sound to synapse* (Oxford University Press, New York, 1998).
3. Parsons, T.D., Lenzi, D., Almers, W. & Roberts, W.M. Calcium-triggered exocytosis and endocytosis in an isolated presynaptic cell: capacitance measurements in saccular hair cells. *Neuron* **13**, 875-883 (1994).
4. Moser, T. & Beutner, D. Kinetics of exocytosis and endocytosis at the cochlear inner hair cell afferent synapse of the mouse. *Proc Natl Acad Sci U S A* **97**, 883-888 (2000).
5. Schnee, M.E., Lawton, D.M., Furness, D.N., Benke, T.A. & Ricci, A.J. Auditory hair cell-afferent fiber synapses are specialized to operate at their best frequencies. *Neuron* **47**, 243-254 (2005).
6. Griesinger, C.B., Richards, C.D. & Ashmore, J.F. Fast vesicle replenishment allows indefatigable signalling at the first auditory synapse. *Nature* **435**, 212-215 (2005).
7. Keen, E.C. & Hudspeth, A.J. Transfer characteristics of the hair cell's afferent synapse. *Proc Natl Acad Sci U S A* **103**, 5537-5542 (2006).
8. Goutman, J.D. & Glowatzki, E. Time course and calcium dependence of transmitter release at a single ribbon synapse. *Proc Natl Acad Sci U S A* **104**, 16341-16346 (2007).
9. von Gersdorff, H. & Matthews, G. Depletion and replenishment of vesicle pools at a ribbon-type synaptic terminal. *J. Neurosci.* **17**, 1919-1927 (1997).
10. Gomis, A., Burrone, J. & Lagnado, L. Two actions of calcium regulate the supply of releasable vesicles at the ribbon synapse of retinal bipolar cells. *J. Neurosci.* **19** (1999).
11. Zenisek, D., Steyer, J.A. & Almers, W. Transport, capture and exocytosis of single synaptic vesicles at active zones. *Nature* **406**, 849-854 (2000).
12. Thoreson, W.B., Rabl, K., Townes-Anderson, E. & Heidelberger, R. A highly Ca2+-sensitive pool of vesicles contributes to linearity at the rod photoreceptor ribbon synapse. *Neuron* **42**, 595-605 (2004).
13. Rabl, K., Cadetti, L. & Thoreson, W.B. Kinetics of exocytosis is faster in cones than in rods. *J Neurosci* **25**, 4633-4640 (2005).
14. Singer, J.H. & Diamond, J.S. Vesicle depletion and synaptic depression at a mammalian ribbon synapse. *J Neurophysiol* **95**, 3191-3198 (2006).
15. Jackman, S.L.*, et al.* Role of the synaptic ribbon in transmitting the cone light response. *Nat Neurosci* **12**, 303-310 (2009).
16. Hosoi, N., Sakaba, T. & Neher, E. Quantitative analysis of calcium-dependent vesicle recruitment and its functional role at the calyx of Held synapse. *J Neurosci* **27**, 14286-14298 (2007).
17. Saviane, C. & Silver, R.A. Fast vesicle reloading and a large pool sustain high bandwidth transmission at a central synapse. *Nature* **439**, 983-987 (2006).
18. Khimich, D.*, et al.* Hair cell synaptic ribbons are essential for synchronous auditory signalling. *Nature* **434**, 889-894 (2005).

19. Moser, T., Neef, A. & Khimich, D. Mechanisms underlying the temporal precision of sound coding at the inner hair cell ribbon synapse. *J Physiol* **576**, 55-62 (2006).
20. Wittig, J.H., Jr. & Parsons, T.D. Synaptic ribbon enables temporal precision of hair cell afferent synapse by increasing the number of readily releasable vesicles: a modeling study. *J Neurophysiol* **100**, 1724-1739 (2008).
21. Eisen, M.D., Spassova, M. & Parsons, T.D. Large releasable pool of synaptic vesicles in chick cochlear hair cells. *J Neurophysiol* **91**, 2422-2428 (2004).
22. Johnson, S.L., Marcotti, W. & Kros, C.J. Increase in efficiency and reduction in Ca2+ dependence of exocytosis during development of mouse inner hair cells. *J Physiol* **563**, 177-191 (2005).
23. Roux, I.*, et al.* Otoferlin, defective in a human deafness form, is essential for exocytosis at the auditory ribbon synapse. *Cell* **127**, 277-289 (2006).
24. Roux, I.*, et al.* Myosin VI is required for the proper maturation and function of inner hair cell ribbon synapses. *Hum Mol Genet* **18**, 4615-4628 (2009).
25. Heidrych, P.*, et al.* Otoferlin interacts with myosin VI: implications for maintenance of the basolateral synaptic structure of the inner hair cell. *Hum Mol Genet* **18**, 2779-2790 (2009).
26. Schwander, M.*, et al.* A forward genetics screen in mice identifies recessive deafness traits and reveals that pejvakin is essential for outer hair cell function. *J Neurosci* **27**, 2163-2175 (2007).
27. Brandt, A., Khimich, D. & Moser, T. Few CaV1.3 channels regulate the exocytosis of a synaptic vesicle at the hair cell ribbon synapse. *J Neurosci* **25**, 11577-11585 (2005).
28. Frank, T., Khimich, D., Neef, A. & Moser, T. Mechanisms contributing to synaptic Ca2+ signals and their heterogeneity in hair cells. *Proc Natl Acad Sci U S A* **106**, 4483-4488 (2009).
29. Spassova, M.A.*, et al.* Evidence that rapid vesicle replenishment of the synaptic ribbon mediates recovery from short-term adaptation at the hair cell afferent synapse. *J Assoc Res Otolaryngol* **5**, 376-390 (2004).
30. Meyer, A.C.*, et al.* Tuning of synapse number, structure and function in the cochlea. *Nat Neurosci* **12**, 444-453 (2009).
31. Li, G.L., Keen, E., Andor-Ardo, D., Hudspeth, A.J. & von Gersdorff, H. The unitary event underlying multiquantal EPSCs at a hair cell's ribbon synapse. *J Neurosci* **29**, 7558-7568 (2009).
32. Glowatzki, E. & Fuchs, P.A. Transmitter release at the hair cell ribbon synapse. *Nat Neurosci* **5**, 147-154 (2002).
33. Grant, L., Yi, E. & Glowatzki, E. Two modes of release shape the postsynaptic response at the inner hair cell ribbon synapse. *J Neurosci* **30**, 4210-4220.
34. Taberner, A.M. & Liberman, M.C. Response properties of single auditory nerve fibers in the mouse. *J Neurophysiol* **93**, 557-569 (2005).
35. Strenzke, N.*, et al.* Complexin-I is required for high-fidelity transmission at the endbulb of held auditory synapse. *J Neurosci* **29**, 7991-8004 (2009).
36. Starr, A., Michalewski, H.J., Feng, G. & Moser, T. Perspectives on auditory neuropathy: disorders of inner hair cell, auditory nerve and their

synapse. in *The Senses: A comprehensive reference* (ed. P.D.a.D. Oertel.) 397–412 (Elsevier, Amsterdam 2008).
37. Obholzer, N.*, et al.* Vesicular glutamate transporter 3 is required for synaptic transmission in zebrafish hair cells. *J Neurosci* **28**, 2110-2118 (2008).
38. Seal, R.P.*, et al.* Sensorineural deafness and seizures in mice lacking vesicular glutamate transporter 3. *Neuron* **57**, 263-275 (2008).
39. Ruel, J.*, et al.* Impairment of SLC17A8 encoding vesicular glutamate transporter-3, VGLUT3, underlies nonsyndromic deafness DFNA25 and inner hair cell dysfunction in null mice. *Am J Hum Genet* **83**, 278-292 (2008).
40. Hosoi, N., Holt, M. & Sakaba, T. Calcium dependence of exo- and endocytotic coupling at a glutamatergic synapse. *Neuron* **63**, 216-229 (2009).
41. Wadel, K., Neher, E. & Sakaba, T. The coupling between synaptic vesicles and Ca2+ channels determines fast neurotransmitter release. *Neuron* **53**, 563-575 (2007).
42. Wolfel, M., Lou, X. & Schneggenburger, R. A mechanism intrinsic to the vesicle fusion machinery determines fast and slow transmitter release at a large CNS synapse. *J Neurosci* **27**, 3198-3210 (2007).
43. Neef, J.*, et al.* The Ca2+ channel subunit beta2 regulates Ca2+ channel abundance and function in inner hair cells and is required for hearing. *J Neurosci* **29**, 10730-10740 (2009).
44. de Wit, H.*, et al.* Synaptotagmin-1 docks secretory vesicles to syntaxin-1/SNAP-25 acceptor complexes. *Cell* **138**, 935-946 (2009).
45. Sterling, P. & Matthews, G. Structure and function of ribbon synapses. *Trends Neurosci* **28**, 20-29 (2005).
46. Dulon, D., Safieddine, S., Jones, S.M. & Petit, C. Otoferlin is critical for a highly sensitive and linear calcium-dependent exocytosis at vestibular hair cell ribbon synapses. *J Neurosci* **29**, 10474-10487 (2009).
47. Beutner, D., Voets, T., Neher, E. & Moser, T. Calcium dependence of exocytosis and endocytosis at the cochlear inner hair cell afferent synapse. *Neuron* **29**, 681-690. (2001).
48. Neef, A.*, et al.* Probing the mechanism of exocytosis at the hair cell ribbon synapse. *J Neurosci* **27**, 12933-12944 (2007).
49. Goodman, M.B. & Lockery, S.R. Pressure polishing: a method for re-shaping patch pipettes during fire polishing. *J Neurosci Methods* **100**, 13-15 (2000).
50. McCue, M. & Guinan, J., Jr. Acoustically responsive fibers in the vestibular nerve of the cat. *J. Neurosci.* **14**, 6058-6070 (1994).

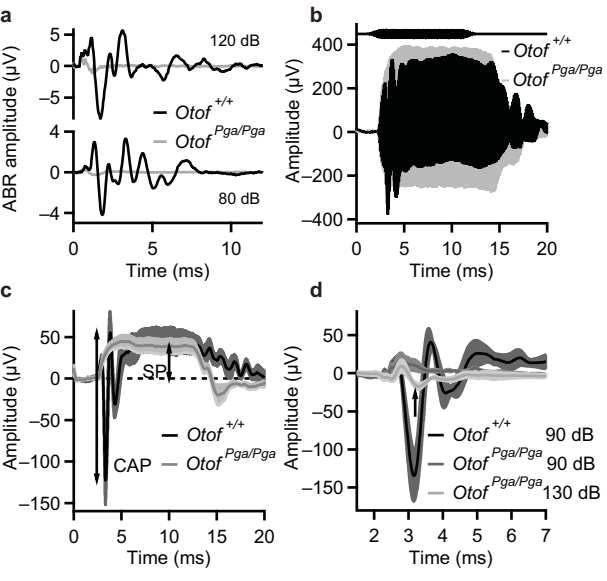
a
120 dB
80 dB
Otof +/+
Otof Pga/Pga
ABR amplitude (μV)
Time (ms)
b
Otof +/+
Otof Pga/Pga
Amplitude (μV)
Time (ms)
c
SP
CAP
Otof +/+
Otof Pga/Pga
Amplitude (μV)
Time (ms)
d
Otof +/+ 90 dB
Otof Pga/Pga 90 dB
Otof Pga/Pga 130 dB
Amplitude (μV)
Time (ms)

Figure 1

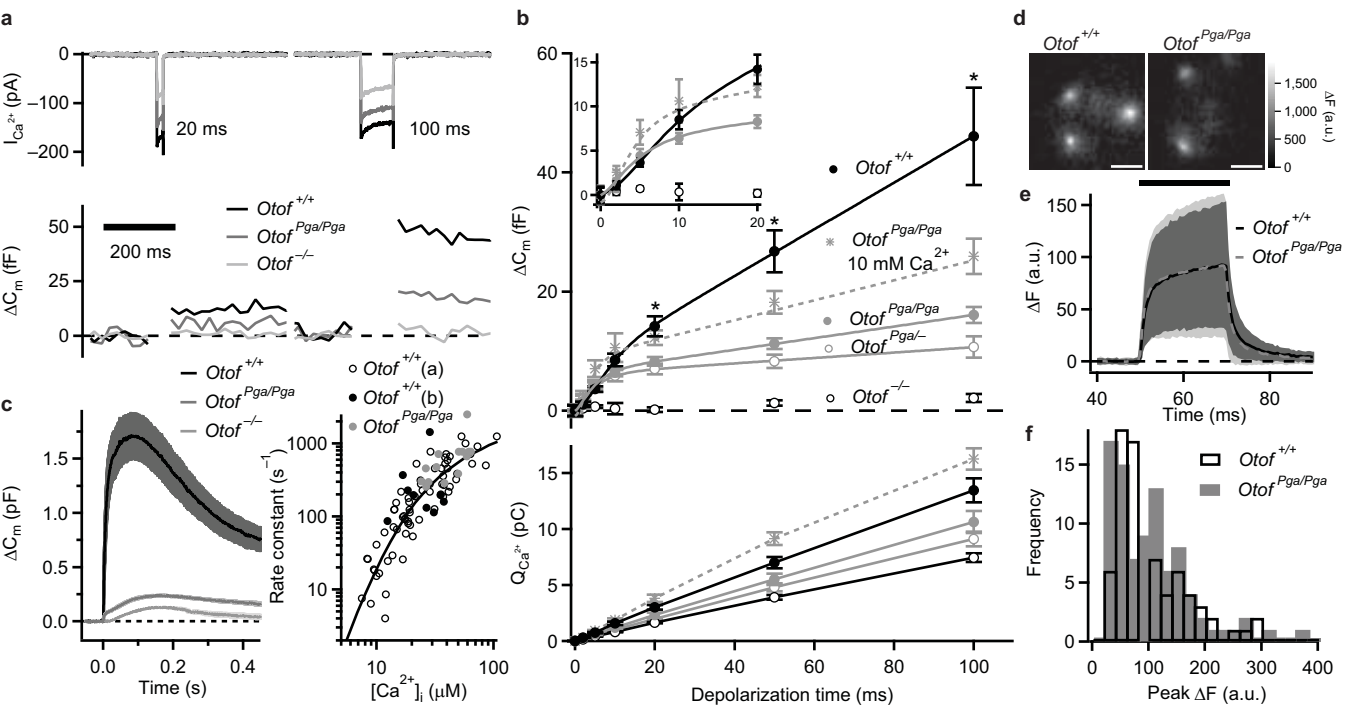
a
b
c
d
e
f
20 ms
100 ms
200 ms
Otof +/+
Otof Pga/Pga
Otof −/−
Otof Pga/–
10 mM Ca2+
Time (s)
Time (ms)
Depolarization time (ms)
Peak ΔF (a.u.)
Frequency
Rate constant (s−1)
[Ca2+]i (μM)
Otof +/+ (a)
Otof +/+ (b)

Figure 2

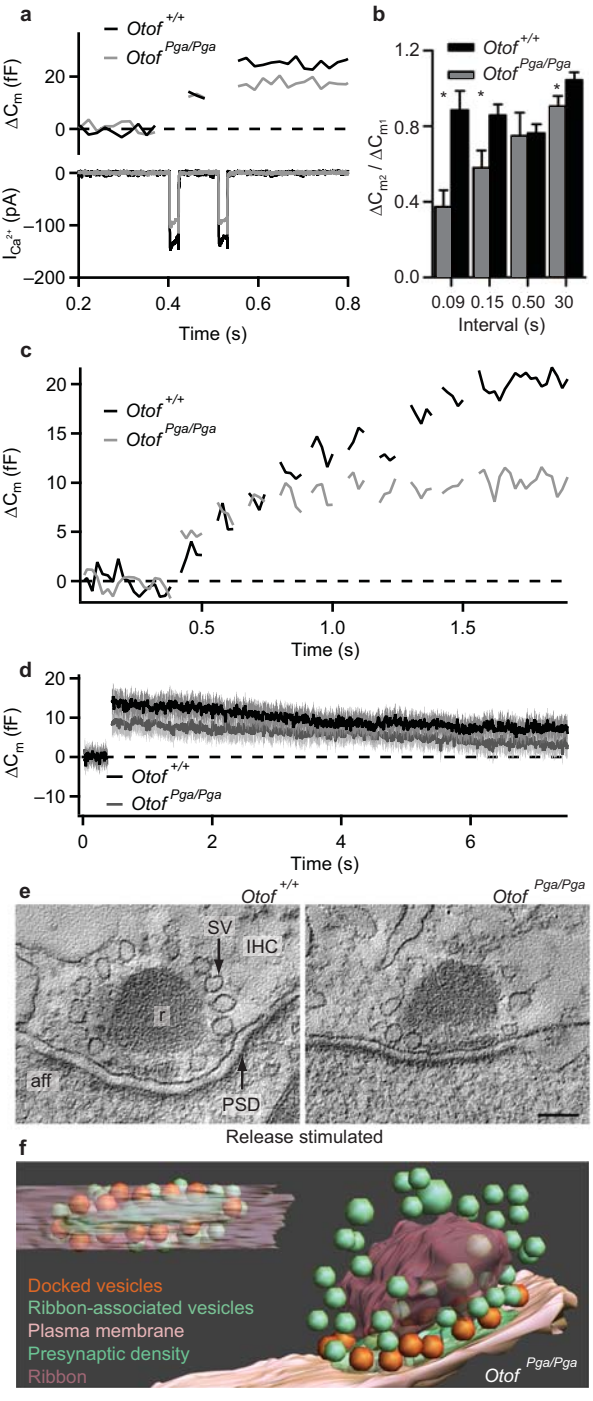
a
Otof +/+
Otof Pga/Pga
ΔCm (fF)
20
0
0
−100
−200
ICa2+ (pA)
0.2
0.4
0.6
0.8
Time (s)
b
Otof +/+
Otof Pga/Pga
1.2
0.8
0.4
0.0
ΔCm2 / ΔCm1
*
*
*
0.09 0.15 0.50 30
Interval (s)
c
Otof +/+
Otof Pga/Pga
ΔCm (fF)
20
15
10
5
0
0.5
1.0
1.5
Time (s)
d
ΔCm (fF)
20
10
0
−10
Otof +/+
Otof Pga/Pga
0
2
4
6
Time (s)
e
Otof +/+
Otof Pga/Pga
SV
IHC
r
aff
PSD
Release stimulated
f
Docked vesicles
Ribbon-associated vesicles
Plasma membrane
Presynaptic density
Ribbon
Otof Pga/Pga

Figure 3

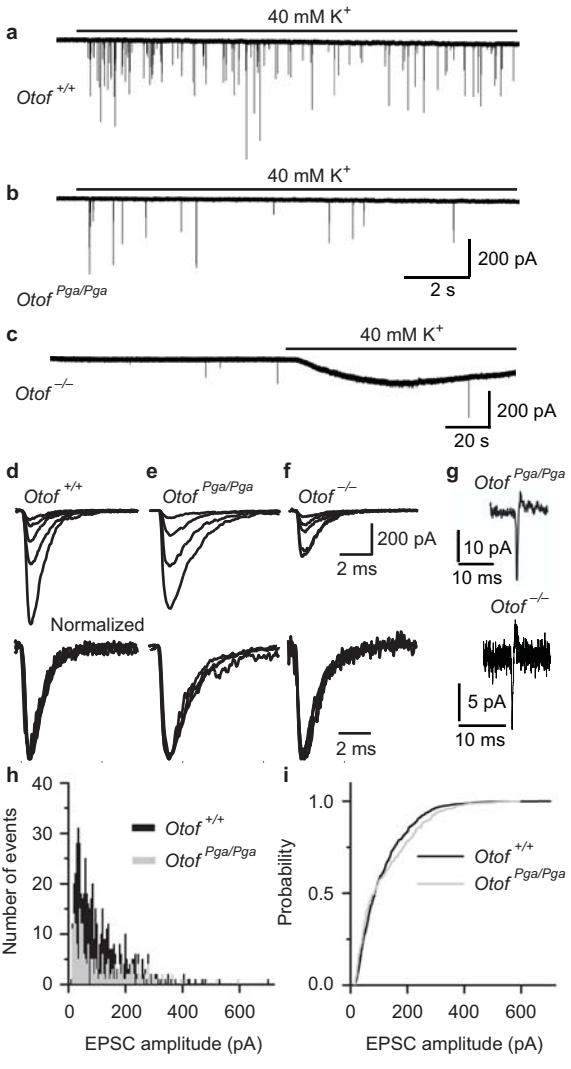
a
40 mM K+
Otof +/+
b
40 mM K+
200 pA
2 s
Otof Pga/Pga
c
40 mM K+
Otof −/−
200 pA
20 s
d
Otof +/+
e
Otof Pga/Pga
f
Otof −/−
200 pA
2 ms
g
Otof Pga/Pga
10 pA
10 ms
Otof −/−
5 pA
10 ms
Normalized
2 ms
h
Number of events
Otof +/+
Otof Pga/Pga
EPSC amplitude (pA)
i
Probability
Otof +/+
Otof Pga/Pga
EPSC amplitude (pA)

Figure 4

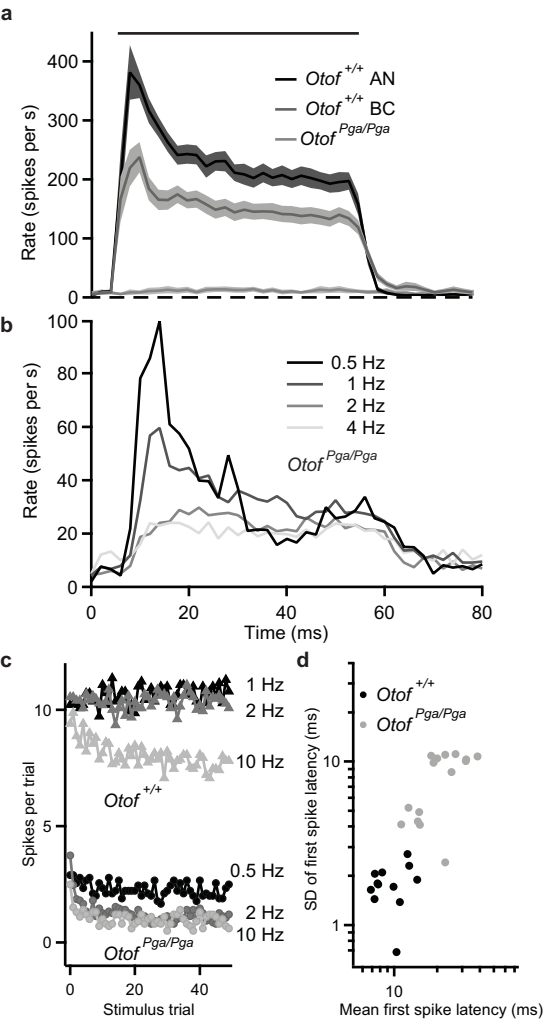
a
Rate (spikes per s)
Otof +/+ AN
Otof +/+ BC
Otof Pga/Pga
b
Rate (spikes per s)
0.5 Hz
1 Hz
2 Hz
4 Hz
Otof Pga/Pga
Time (ms)
c
Spikes per trial
1 Hz
2 Hz
10 Hz
Otof +/+
0.5 Hz
2 Hz
10 Hz
Otof Pga/Pga
Stimulus trial
d
Otof +/+
Otof Pga/Pga
SD of first spike latency (ms)
Mean first spike latency (ms)

Figure 5

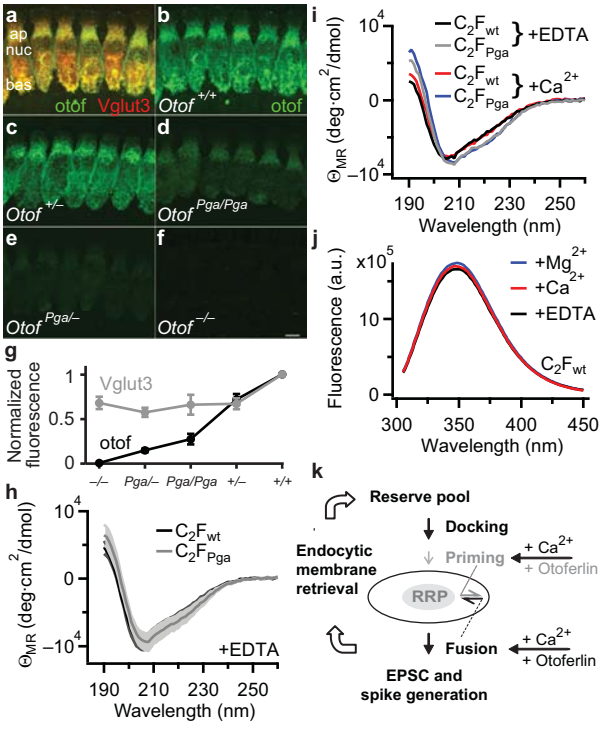
a
ap
nuc
bas
otof Vglut3
b
Otof +/+
otof
c
Otof +/–
d
Otof Pga/Pga
e
Otof Pga/–
f
Otof –/–
g
Normalized fluorescence
Vglut3
otof
–/– Pga/– Pga/Pga +/– +/+
h
C2Fwt
C2FPga
+EDTA
ΘMR (deg·cm2/dmol)
Wavelength (nm)
i
C2Fwt
C2FPga
+EDTA
+Ca2+
ΘMR (deg·cm2/dmol)
Wavelength (nm)
j
x10 5
+Mg2+
+Ca2+
+EDTA
C2Fwt
Fluorescence (a.u.)
Wavelength (nm)
k
Reserve pool
Docking
Priming
+ Ca2+
+ Otoferlin
Endocytic membrane retrieval
RRP
Fusion
+ Ca2+
+ Otoferlin
EPSC and spike generation

Figure 6